International Journal of Fatigue 186 (2024) 108406

Contents lists available at ScienceDirect

International Journal of Fatigue

journal homepage: www.elsevier.com/locate/ijfatigue

A study on the influence of impurity content on fatigue endurance in a 6082 Al-alloy

Aritra Sarkar [a,*], Mehmet Aktunali [a], Siri Marthe Arbo [b], Jon Holmestad [b], Luigi Mario Viespoli [c], Bård Nyhus [c], Geir Ringen [a], Nima Razavi [a]

[a] Department of Mechanical and Industrial Engineering, Norwegian University of Science and Technology, Trondheim, Norway
[b] SINTEF Manufacturing, Raufoss, Norway
[c] SINTEF Industry, Trondheim, Norway

ARTICLE INFO

Keywords:
HCF
Crack initiation
Intermetallic particles
Al-alloys

ABSTRACT

The paper investigates the influence of different impurity/scrap elements on the high cycle fatigue (HCF) properties of 6082 Al-alloy. Accordingly, HCF tests are carried out on the different variants- GA1, GA2 and GA3 (designed as a function of varying impurity content)- of this alloy, which resulted in a lower fatigue limit in GA2/GA3 compared to GA1. To explain such behavior, detailed fractographic and microstructural investigations are conducted which bring out that although the crack initiation and propagation modes are mostly transgranular irrespective of alloy variant and stress levels, intergranular crack initiation is promoted in GA2/GA3 at 150 MPa in contrast to occurrence of run-out in GA1 at the same stress level. This phenomenon is found to be facilitated by intermetallic particles anchoring the grain boundaries. These observations point out the possibility of strong sensitivity of stress and alloy variant (varying impurity content) to fatigue life. The difference in fatigue properties as a function of alloy variant could be attributed to the variation in initial microstructure/particle size distribution as well as the slip character. In light of these, a fracture mechanism map is generated which underlines the different mechanisms responsible for fatigue crack initiation among different alloy variants.

1. Introduction

Aluminium (Al) alloys possess a high strength-to-weight ratio along with excellent corrosion resistance and mechanical properties. This makes them a natural choice for use in the automotive, construction and aerospace industries [1–4]. However, the increasing demand for using primary Al is limited by the high energy costs coupled with emission of greenhouse gases especially when fossil fuels are used for the primary production [5,6]. A viable alternative to this scenario is the usage of secondary Al [6–10]. This is possible by utilizing Al-scrap for producing Al-alloys. In this route wherein the scrap Al is remelted to produce Al-alloys (secondary Al), the energy cost is cut almost by 95 % compared to production of primary Al from ore [6,11]. At the same time, there is a significant reduction in greenhouse gas emission (CO_2 emission in producing secondary Al is about 5 % of that in primary Al) [6,11]. Therefore, it is imperative that a strategy is devised so that recycled Al can be used suitably in the manufacturing industry.

However, the main challenge in achieving this goal is the presence of undesirable impurity elements in scrap Al. The impurity elements present in scrap Al are primarily Fe, Cu and Zn, and also Si, Mn, Cr, Ti etc [12–15] especially if large amounts of scrap are used. Fe is reported to form intermetallics like Al_8Fe_2Si or Al_5Si with Si [12,13], and also $Al_{15}(Fe, Mn)_3Si_2$ with Mn [12,13]. This can lead to the formation of unfavorable microstructure which can have a detrimental impact on the mechanical properties. Moreover, Fe-rich phases like Π-phase with composition of $Al_{18}Fe_2Mg_7Si_{10}$, and ß-phase with a composition of $Al_9Fe_2Si_2$, formed when the Fe-content is high [16]- are reported to be detrimental for monotonic properties owing to their needle-like morphology which can act as metallurgical notch leading to formation of microcracks, thereby facilitating early fracture [17]. Increase in Fe content is reported to increase the length of the needles in these phases [17], which could be detrimental not only for the monotonic, but especially for the fatigue properties. In this context, it is important to remember that almost 90 % of the engineering failures are caused by fatigue which makes it an important design criterion [18,19]. Deterioration of fatigue properties therefore could limit the lifetime of the

* Corresponding author.
E-mail address: aritra.sarkar@ntnu.no (A. Sarkar).

https://doi.org/10.1016/j.ijfatigue.2024.108406
Received 1 March 2024; Received in revised form 6 May 2024; Accepted 14 May 2024
Available online 15 May 2024

components where secondary Al alloys re-produced from the scrap are used. However, in the current scenario, the information on the effect of impurities on fatigue behavior of recycled Al-alloys is highly limited.

It is reported by Taylor et al. [12] that Fe-based intermetallics (as mentioned above) negatively affect both the tensile strength and ductility in an Al-Si casting alloy. The reduction in ductility is attributed to the formation of porosities by these intermetallics [12]. The porosities are also found to fracture easily under tensile loading, leading to initiation of micro-cracks, thereby causing a reduction in tensile strength [12]. Kim et al. [20] reported wide differences in fatigue properties between low and high cycle fatigue (LCF & HCF) in a AC2B T6 Al casting alloy, with increase in Fe content. Although Si is a common alloying element in Al-alloys, presence of high Fe-content is found to change the morphology of eutectic Si particles from round to needle-like- apart from the formation of Al-Fe intermetallics- which makes the Si particles detrimental for fatigue properties [20]. The fatigue life was found to be lower in the LCF regime which was attributed to the reduction in the dynamic fracture toughness; on the other hand, fatigue life was found to improve in the HCF regime due to the crack deflection by the Al-Fe based intermetallics – which increase with increase in Fe-content [20]. In this context, use of Ca as an alloying addition was found to be useful which led to refinement of the above phases by spheroidization [20]. On a similar note, Zavodska et al. [21] have shown a differential fatigue behavior in the LCF and HCF regime, in the self-hardenable $AlZn_{10}Si_8Mg$ cast alloy, with different levels of Fe-content. In this case, the reduction in fatigue life at higher stresses- with increase in Fe content- was reported to be caused by porosities formed along needle-like Al_5FeSi phases, which prepones the crack initiation [21]. On the other hand, with a similar increase in Fe content, the Al_5FeSi phases supposedly deflect the cracks in the low-stress HCF regime, thereby increasing the fatigue life [21]. Attempts to neutralize the detrimental effects caused by Al-Fe intermetallic on fatigue life was made in terms of small addition of Sr in a AC4A as-cast Al-alloy, which was found to enhance the fatigue properties [22]. This was primarily attributed to the delayed crack propagation caused by refinement of the needle-like eutectic Si phase to a fibrous morphology and coarser Al-Fe intermetallics to a finer morphology [22]. In case of spray formed AA7050 alloy, a solution heat-treatment followed by artificial aging at 120 °C for 6 h, after rotary swaging, was found to enhance the fatigue properties [23]. This was attributed to the homogenization of the microstructure and dissolution of coarser intermetallics during the solutionizing procedure, which presumably minimized the chances of fatigue crack initiation [23]. The subsequent ageing treatment led to formation of coherent and semi-coherent GP(I) zones and η′phase, which reduced the crack growth rate, leading to improved fatigue life [23].

In a similar line, a few studies carried out in AW6082 and AW6060 Al-alloy recycled by SSR (solid-state recycling) showed inferior fatigue properties compared to the reference material [24–26]. This was attributed to the formation of chip delaminates with poor bonding strength during the process of SSR, which acted as potential sites for early crack nucleation. [24–26]. Since SSR does not involve remelting and consequent formation of liquid phases, Fe-rich phases do not form during SSR. Therefore, chip delaminates are the major detriment towards fatigue properties under SSR unlike remelting process wherein Fe-rich phases that formed are the more damaging ones. ECAP (Equal Channel Angular Pressing) treatment was found to result in better fatigue properties in the same AW6082 alloy processed by SSR, which was attributed to the significant improvement in the bonding strength between the aluminum chips which delayed the crack propagation along the delaminated chip boundaries [26].

The above discussion makes it clear that in view of the scarcity of the literature available in this subject, a thorough understanding is required on how these impurities affect the fatigue behavior of the recycled Al-alloys. Moreover, the existing literature did not properly address how fatigue failure mechanisms change with increase in impurity content- there is a definite lack of detailed fractographic investigation-and what precisely is the role of the microstructural changes (change in slip character?) associated with an increase in impurity content on fatigue life. This calls for a detailed investigation on high cycle fatigue (HCF) behavior of recycled Al-alloy which can address the above issues towards formulating necessary measures to mitigate the possible harmful impact of the impurities on fatigue life. The material chosen for the present study is a 6082 Al-alloy, with Mg and Si as the primary alloying elements. This alloy belongs to the 6xxx series of Al-alloys which are heat-treatable and possess an excellent combination of strength, formability and corrosion resistance [27,28]. Among other Al-alloys in the 6xxx series, 6082 Al-alloy possesses the highest strength which makes it an obvious choice for use in the structural and automobile components [27,28]. In the present case, the 6082 Al-alloy is designed specifically with varying scrap contents so that it can simulate the actual recycled alloy produced from post-consumer-scrap. Three variants are chosen, and designated as GA1, GA2 and GA3 with increasing level of impurities like Fe, Cu, Zn etc. The effect of the intermetallics formed on account of these impurities, on fatigue life, and more precisely on fatigue crack initiation is assessed by correlating the fatigue data with fracture surface investigation and microstructural evaluation. The microstructural variations caused by the intermetallics will change with the impurity content, which can bring about difference in fatigue properties among the alloy variants, with respect to the applied stress. The above aspects are investigated in detail in the present study, towards providing a roadmap for recyclability-oriented alloy design wherein the allowable/maximum amount of scrap content can be optimized based on fatigue properties.

2. Materials and methods

2.1. Material used and processing route

The material used in the present study is AA6082 Al-alloy manufactured by Norsk Hydro ASA. The material is available in three variants designated as GA1, GA2 and GA3 (with increasing level of impurities). The chemical composition of the three variants is shown in Table 1.

The alloy is manufactured through GC (Gas cushioning) casting followed by homogenization at 580 °C for 2 hrs. and 15 mins. The cast material is hot extruded in 700 mm long billets using solid die for each variant at 480°C employing a puller speed of 11.8 mm/min. In total, 168 presses are performed to complete the extrusion process with 14 presses per variant and die. Post-extrusion, cooling is performed by water-spraying followed by 1 % stretching. Then, a T6 temper is carried out by aging at 175 °C for 5.5 hrs. The homogenization treatment is performed prior to extrusion to ensure that any potential inhomogeneities after casting is removed and the billet could achieve the desired microstructure without compromising the extrusion speed.

In the present work which is focused on fatigue properties, tensile tests are conducted primarily to determine the yield strength and ultimate tensile strength which are important indicators to ascertain the stresses to be considered for fatigue tests. In the tensile tests, one specimen is used for each variant. The tests are conducted on profiles transverse to the extrusion direction in an electromechanical testing machine Zwick/Roell Z250 (250 kN) under displacement-controlled mode according to ASTM E8 [29] using an extensometer for strain measurement which is calibrated according to ISO 9513:2012 class 0.5. The geometry of the tensile specimen is shown in Fig. 1(a).

2.2. Fatigue tests

Smooth fatigue specimens are machined from the extruded profiles transverse to the extrusion direction with a flat geometry (using gage length of 20 mm, gage diameter of 10 mm and thickness of 6 mm, see Fig. 1(b)). The choice of flat specimens over cylindrical geometries is made to retain the as-built surface condition and the parent microstructure present on the surface of the extruded profiles. For easy comparison of the test results in the present work with that of weld-

Table 1
Chemical composition of the different alloy variants (wt%).

Designation	Si	Fe	Cu	Mn	Mg	Cr	Zn	Ti	Al
GA1	0.9	0.22	0.02	0.55	0.65	–	0.02	0.01	
GA2	0.9	0.28	0.05	0.55	0.65	–	0.1	0.01	Balance
GA3	0.9	0.32	0.1	0.55	0.65	–	0.2	0.01	

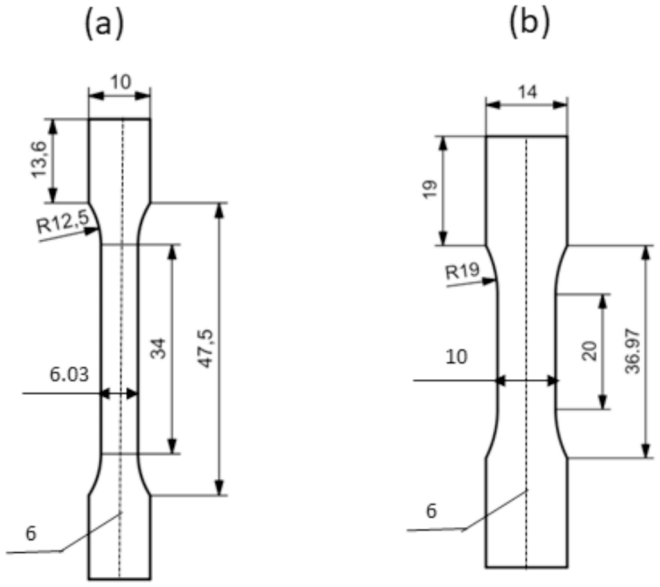

Fig. 1. Specimen geometry for (a) tensile tests (b) fatigue tests. Unit: mm (not to scale)

joints, the specimens are designed in such a way that the thickness to width ratio in the geometry is similar to that in the weld-joint.

Uniaxial high cycle fatigue (HCF) tests are carried out on the specimens in a servo-electric fatigue testing system (STEPLAB) equipped with a 20 kN load cell. All tests are carried out at ambient temperature, under load-controlled mode, employing a sinusoidal waveform, with a test frequency of 25 Hz and load-ratio $R = 0.1$. The run-out limit is set as 2×10^6 cycles. The test matrix (refer Table 2) is kept similar for all the alloy variants with 9 tests for each *S-N* curve, to compare the fatigue data in a one-to-one scale.

2.3. Fractography and metallography

Fractographic and metallographic investigations are presented only for the alloy variants GA1 and GA3 to portray the extreme conditions. The fracture surface of the failed specimens is investigated using scanning electron microscope (SEM) (FEI, Quanta™ 650 FEG) coupled with EDS (energy dispersive spectroscopy) to gain a deeper understanding of failure mechanisms, as a function of different stresses and alloy variants. To reveal the microstructure of the as-extruded profile, an anodization treatment is carried out using Barkers Reagent (5 % HBF4 in water, 20 V for 60 sec). Low-resolution images are obtained using optical microscope Leica DMI 5000 M under polarized light settings using the software Imagepro. High resolution images are obtained using a Hitachi S-3500N SEM with a tungsten filament equipped with an Oxford X-Max system operating at 20 kV accelerating voltage.

2.4. Electron back-scattered diffraction (EBSD)

EBSD analysis is performed only on the as-extruded samples (in the edge region containing the recrystallized grains) from the alloy variants GA1 and GA3. Samples for the EBSD studies are prepared by conventional metallographic method followed by ion milling at 4 V in 30 min in a Hitachi IM4000 Plus ion milling system. The substructure is characterized employing a Hitachi S-3500N SEM with a tungsten filament equipped with an Oxford X-Max system operating at 20 kV accelerating

Table 2
Matrix showing the fatigue test details and results for different Alloy variants.

Designation	Maximum stress (MPa)	Cycles to failure	Repetitions	Used for generating mean strain data	Used for fractography
GA1	270	65,159	3	X	X
		22,132			
		127,741			
	220	214,995	2		
		99,998			
	180	568,076	2	X	
		492,579			
	150	2,000,000	2	X	
		2,000,000			
GA2	270	49,791	2		
		40,925			
	220	125,699	2		
		111,960			
	180	161,738	2		
		229,727			
	150	874,594	2		
		629,360			
	120	2,000,000	1		
GA3	270	59,901	2		
		45,114		X	X
	220	134,112	2		
		83,664			
	180	153,070	2		
		261,332		X	X
	150	604,734	2		
		1,364,986		X	X
	120	2,000,000	1		

voltage, and 120 μm objective aperture. The scans are performed using a step size of 0.5–3 μm depending on the grain size. TSL OIM™ software is utilized to analyze the EBSD data and consequently, crystal orientation/inverse pole figure (IPF) map, and Schmid factor map are generated. As per the software guidelines, minimum 2 pixels is considered to define a grain for reliable statistics.

3. Results

3.1. Initial microstructure

Representative microstructures of the final extruded material available as solid flat profile, pertaining to alloy variant GA3 are shown in Fig. 2. A recrystallized layer with larger grains is observed in the edge (surface), with a fibrous region (extruded zone) in the centre. The alloy variant GA1 shows similar microstructural features and therefore is not shown. Representative microstructural images taken from both the edge and centre show presence of intermtallic primary particles (marked by arrow in the figure).

The grain size distribution for both the alloy variants in edge (recrystallized region) as well as centre (extruded region), are presented in Fig. 3(a)-(b). The grain size distribution and average grain size is measured using the TSL OIM™ software. The areas are taken randomly from edge and centre, but the grain overview images show that there are no/minor differences based on where the measurement is taken. The corresponding average grain size is found to be much higher at the edge compared to the centre (see Table 3(a)). This is attributed to the presence of recrystallized grains at the edge which varies widely in size from as small as ~ 25 μm to as big as ~ 340 μm. The recrystallized grains are formed during the homogenization treatment before extrusion, but they experience grain growth during the extrusion process. During the extrusion process, the edge region experiences a high degree of non-uniform deformation coupled with a high temperature gradient which results in abnormal grain growth upto ~ 340 μm in some of the recrystallized grains present at the edge.

The particle size distribution is calculated using the software ImageJ with minimum particle size of 0.4 um^2 (based on 6 images randomly taken from both centre and edge) and presented in Fig. 4. The corresponding average particle size is found to be slightly higher at the centre compared to the edge, irrespective of the alloy variant (see Table 3(b)). This is attributed to the higher degree of deformation experienced by the edge region compared to that at the centre during the extrusion process. This leads to breaking up of particles at the edge resulting in smaller particle size therein compared to that at centre.

The number density follows an opposite trend with higher at the edge compared to the centre. Moreover, the number-density is found to be significantly higher in GA3 compared to GA1, especially at the edge where the value is found to be almost double of that found in GA1. To find out the exact specification of the particles, EDS spectrums are taken randomly at different locations at the centre (see Table 4) which reveals that the particles are primarily Al-rich (~80 %) along with Fe, Mn and Si and therefore can be designated as Al-Fe-Mn-Si intermetallics. For better clarification, a representative SEM image pertaining to the alloy variant GA1 showing the eight locations of EDS spectra along with a spectrum image (spectrum 4) is added in the Appendix A (see Fig. A1).

3.2. Fatigue properties

Fig. 5 (a-c) shows the S-N curves determined from the fatigue test results. The corresponding test data is tabulated in Table 2. The stresses considered for fatigue tests are determined based on the tensile properties (see Table 5). Both the yield strength (YS) and ultimate tensile strength (UTS) are found to increase slightly from GA1 (YS: 310 MPa, UTS: 336 MPa) to GA3 (YS: 325 MPa, UTS: 349 MPa) with a marginal decrease in ductility (12 % in GA1 and 11 % in GA3). Accordingly, the stresses used in fatigue tests are kept lower than YS for the respective variants.

To take into account the statistical nature of fatigue data, a probabilistic analysis is carried out and lines marked with 10 %, 50 % and 90 % survival probability, along with the inverse slope of the S-N curve, k and the scatter index T_σ (the ratio between the stress amplitudes corresponding to 10 % and 90 % of survival probability) are indicated in the figures. The probabilistic analysis is carried out using a log-normal distribution of the fatigue data following the guidelines of the standard ISO 12107 [30].

Statistical fatigue limit is determined as the corresponding stress amplitude in the probability line of 50 % where the specimen has undergone run-out upto 2 million cycles and marked with an arrow in the figures. Actual fatigue limit is determined as maximum value of the stress which corresponds to run-out upto 2 million cycles. Statistical fatigue limit is found to be lower for the alloy variants GA2 (115 MPa) and GA3 (120 MPa), compared to GA1 (140 MPa). Actual fatigue limit shows a similar trend GA1: 150 MPa, GA2: 120 MPa and GA3:120 MPa. Since the difference between the statistical fatigue limit and the actual fatigue limit is nominal, only the values pertaining to actual fatigue limit will be referred hereafter and will be termed plainly as fatigue limit, to avoid confusion. Fatigue limit is found to be lower for the alloy variants GA2 and GA3 (by 20 %), compared to GA1. To get a clearer understanding on the influence of alloy variants on the fatigue behavior and how the same varies with change in stress, the fatigue test results are

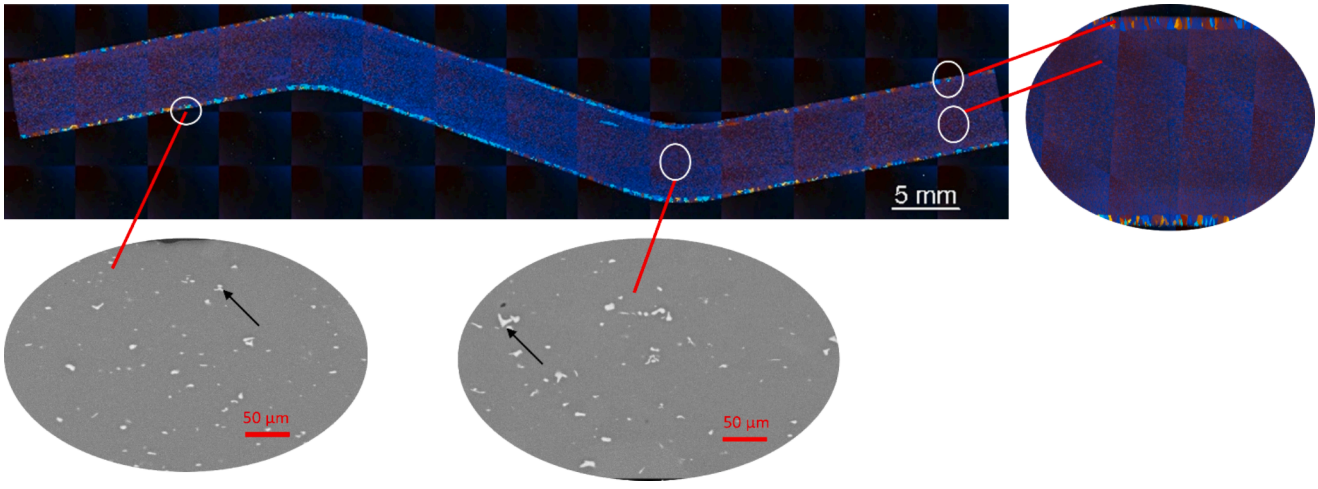

Fig. 2. Microstructure of the alloy variant GA3 showing overall view of the entire profile – recrystallized region at the edge and extruded region at the centre. Magnified view of regions from edge and centre show presence of intermetallic primary particles (marked by black arrows).

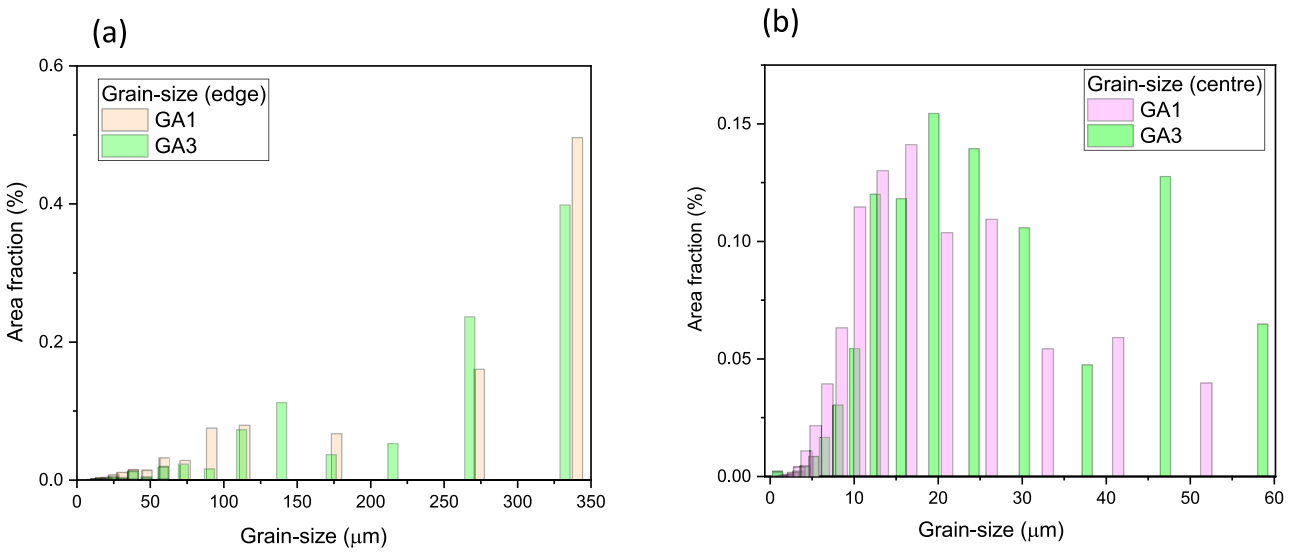

Fig. 3. Grain-size distribution of the alloy variants GA1 and GA3 (a) edge (b) centre.

Table 3
(a) Grain-size distribution (μm) and (b) Particle size distribution (μm) in the Alloy variants GA1 and GA3 at different locations (centre and edge).

(a)		
Location	Designation	Average grain-size
Centre	GA1	24.3 ± 17.5
	GA3	25.8 ± 15.3
Edge	GA1	249.8 ± 121.3
	GA3	250.1 ± 107

(b)				
Location	Designation	Area fraction	Average particle size	Number density
Centre	GA1	1.63±0.15	2.44±2.31	6616±192
	GA3	1.82±0.13	2.19±1.87	8312±347
Edge	GA1	1.41±0.17	1.95±1.97	6995±577
	GA3	1.89±0.22	1.64±1.39	11431±1349

compared in Fig. 6. The 50 % probability line indicates that the fatigue properties are better in GA1 compared to GA2/GA3 wherein the statistical fatigue life is higher. Moreover, the difference in statistical fatigue life between GA1 and GA2/GA3 is more at lower values of stresses. This ultimately results in a higher fatigue limit in GA1 compared to GA2/GA3 (see Figs. 5 and 6). The trend found in Fig. 6 could be explained on the basis of the detrimental aspects of the intermetallics formed in GA2/GA3 in relation to fatigue crack initiation, especially considering the fact that impurity content is higher in GA2/GA3 compared to GA1 (see Table 1). However, this aspect will be dealt further in the latter sections pertaining to fracture surface investigations.

3.3. Variation in cyclic strain

HCF tests are conducted in stress-controlled mode in the present case. The strain experienced under fatigue cycling is plotted as the variation of mean strain (%) with cycle count in Fig. 7. To obtain the mean strain, the displacement undergone by the specimen during cycling stressing is considered. The displacement values are measured directly from the machine and are used mainly for comparing among the alloy variants at different stresses, rather than generating the hysteresis loops.

The loading conditions which are used for calculation of mean strain are marked in Table 2. The figures are presented with % fatigue life rather than actual fatigue life, so that a one-to-one comparison in the trend in strain between different stress-levels and different variants can

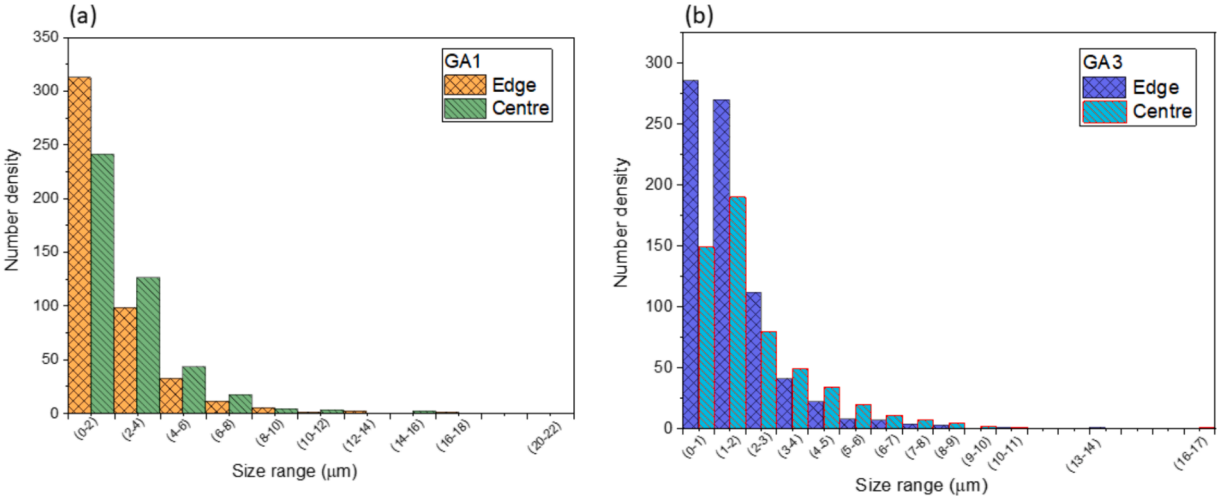

Fig. 4. Particle-size distribution of the alloy variants showing primary particles (a) GA1 (b) GA3.

Table 4
Composition of the particles (in at%) in GA1 and GA3 from the EDS spectrums.

GA1							GA3							Total
Spectrum	Mg	Al	Si	Ti	Mn	Fe	Mg	Al	Si	Mn	Fe	Cu	Zn	
Spectrum 1	7.74	76.80	14.88	0.24	0.34		0.78	98.02	0.86	0.34				100
Spectrum 2	0.4	75.07	6.15		7.97	10.41	0.34	73.52	6.09	6.86	12.66	0.54		100
Spectrum 3	0.58	86.66	3.03		4.22	5.52	0.54	84.81	4.78	3.78	6.09			100
Spectrum 4	0.43	74.89	6.65		9.69	8.34	0.6	87.06	3.26	3.22	5.53	0.32		100
Spectrum 5	0.63	83.02	4.18		6.01	6.17	0.53	83.73	3.97	4.29	7.48			100
Spectrum 6	0.61	89.66	3.37		3.52	2.85	0.43	81.70	5.01	4.81	7.71		0.33	100
Spectrum 7	0.43	76.86	6.20		7.44	9.07	0.56	83.29	5.03	5.63	5.47			100
Spectrum 8	0.65	80.72	5.93	0.83	7.66	4.22	0.46	78.21	5.38	5.18	10.39	0.39		100
Spectrum 9							2.24	94.87	2.46	0.43				100
Spectrum 10							0.40	78.74	5.32	5.52	9.63	0.39		100
Max.	**7.74**	**89.66**	**14.88**	**0.83**	**9.69**	**10.41**	**2.24**	**98.02**	**6.09**	**6.86**	**12.66**	**0.54**	**0.33**	
Min.	**0.4**	**74.89**	**3.03**	**0.24**	**0.34**	**2.85**	**0.34**	**73.52**	**0.86**	**0.34**	**5.47**	**0.32**	**0.33**	

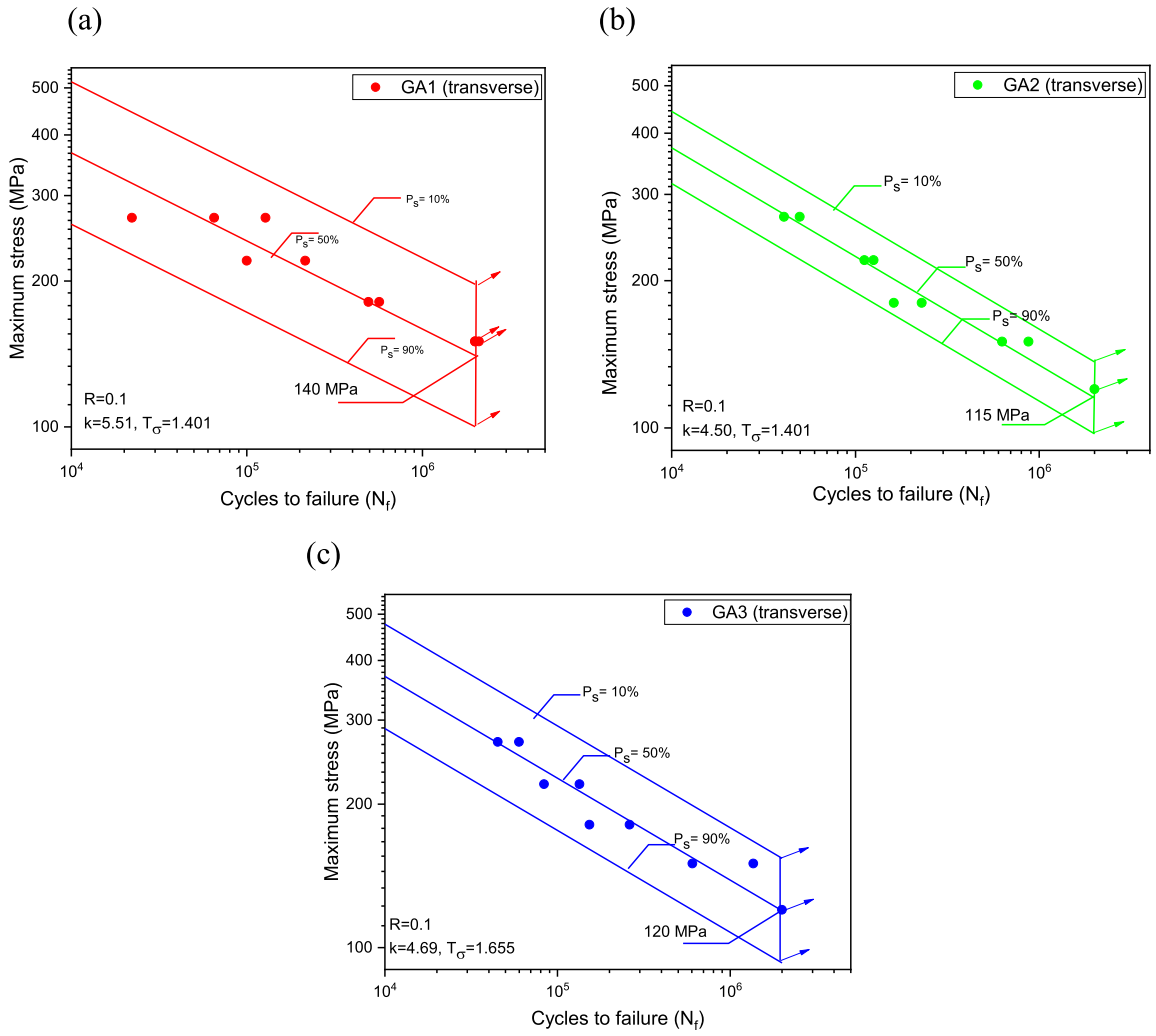

Fig. 5. S-N curves based on HCF tests corresponding to (a) GA1 (b) GA2 (c) GA3 showing different probability lines (10 %, 50 % and 90 %), R = 0.1.

Table 5
Tensile test results for different alloy variants.

Designation	Yield strength (YS), 0.2 % (MPa)	Ultimate tensile strength (UTS) (MPa)	Ductility (% elongation)
GA1	309	331	14
GA3	327	350	11

be made. This also enables to identify and compare the presence and extent of cyclic hardening or softening tendencies at different stages of the fatigue cycling among different stresses and variant.

Since the fatigue properties of GA2 and GA3 are almost similar (see Fig. 6), only two variants GA1 and GA3 are used in Fig. 7. The mean strain plotted in Fig. 7 normally represents elastic strain since HCF deformation is grossly elastic [18,19]. However, some small amount of microplasticity can be observed even under HCF [31–34], leading to small variation in mean strain with progressive cycling. Such plastic

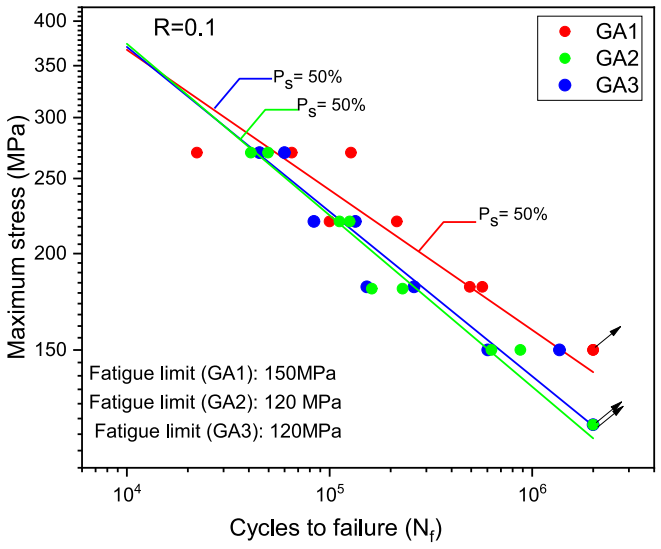

Fig. 6. Comparative S-N curves based on 50 % probability line, R = 0.1.

deformation gets highly localized when microcrack initiates, leading to significant variation (increase) in mean strain towards the end of cycling [31–34].

3.3.1. *Influence of applied stress*

To understand how the applied stress affects the nature of cyclic deformation, the discussion in this section is limited to different stresses (270, 180 & 150 MPa) for a single variant GA3. A continuous increase in cyclic strain is noticed with successive cycling at 270 MPa. The increase is sharp up to 10 % fatigue life, followed by a gradual increase from 10 % to 90 % (see Fig. 7(i)). Beyond 90 % fatigue life, the sharp increase in cyclic strain is an indication of the final crack propagation (Fig. 7(i)). Since the stress remains constant throughout the test, an increase in cyclic strain is indicative of cyclic softening behavior (marked in Fig. 7 (i)), which seems to be quite prominent throughout the fatigue life, at 270 MPa. On further lowering of stress to 180 and 150 MPa, the cyclic strain is found to decrease marginally at the beginning up to 10 % fatigue life, followed by a constant/marginally increasing trend up to 70 % fatigue life, with a gradual increase from 70 % to 90 % fatigue life (this is better understood from Fig. 7(ii) where the scale is adjusted accordingly to magnify the trends corresponding to stress levels 180 & 150 MPa). This indicates a small cyclic hardening tendency at these stress levels (180 and 150 MPa) followed by a cyclic saturation (marked in Fig. 7(ii)).

The high amount of cyclic softening observed at the stress level of 270 MPa almost from the beginning suggests that plastic deformation could be global in this case (see Fig. 7(i)). This is also corroborated from the high amount of strain accrued (~9%, see Fig. 7(i)) up to 90 % life (before final crack propagation) which is quite close to the ductility (~11%, see Table 4). The small amount of cyclic hardening and subsequent cyclic saturation at 180 & 150 MPa (see Fig. 7(ii)) indicates that the deformation in this case is grossly elastic and plastic deformation associated with crack nucleation presumably starts towards the end of cycling (which commensurate with trends found typically under HCF deformation [32,33]. This argument is further supported by the fact that the strain accrued up to 90 % life (before final crack propagation) is found to be quite small (1–1.5 %, see Fig. 7(ii)) for these stress levels (180 & 150 MPa), which is significantly lesser than the ductility (~11%, see Table 4). Moreover, these observations are in line with the previous investigation on a similar AA6082 Al-alloy by Wang et al [35] which shows cyclic hardening characteristic for the majority of fatigue life (without pre-strain) at a stress range of 250 MPa with statistical fatigue life of ~10^5 cycles, under HCF.

3.3.2. *Influence of alloy variant*

The nature of cyclic softening is found to be similar for both the variants GA1 and GA3 at 270 MPa, although the cyclic strain curve for GA3 is slightly higher than that of GA1 see Fig. 7(i)). This is in correlation with the higher fatigue lives in GA1 (65159) compared to GA3 (45114) for the above stress levels. It is important to note that although the statistical fatigue life at 270 MPa is higher for GA1 compared to GA3, the level of scatter at this stress level is quite high resulting in lower fatigue life in GA1 compared to GA3 for one specimen (please refer to Table 2 for the details). At lower stresses like 180 and 150 MPa, the cyclic strain accrued for GA3 is found to be higher than GA1 (see Fig. 7 (ii)), although both the cases show a cyclic hardening tendency followed by cyclic saturation. This is in correlation with the higher fatigue lives in GA1 (568076 at 180 MPa, run-out at 150 MPa) compared to GA3 (261332 at 180 MPa, 1,364,986 at 150 MPa) for the above stress levels and the trend observed in the *S-N* curve observed in Fig. 8. A relatively higher accumulation of strain in GA3 compared to GA1, albeit small, points out the possibility that the ease of slip/tendency of cross-slip is

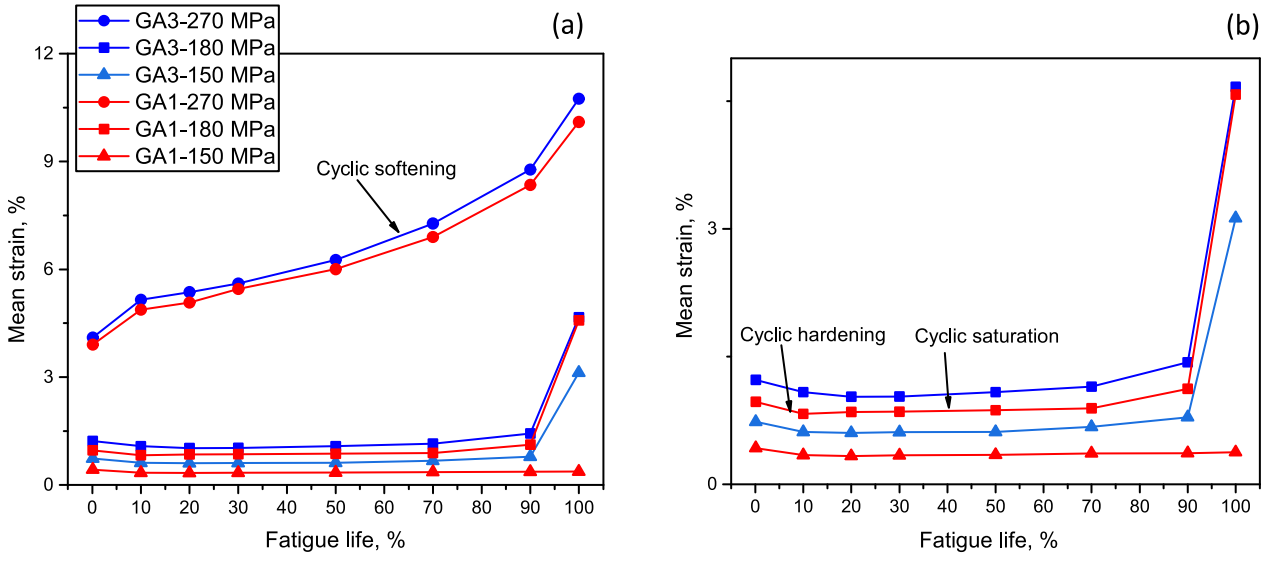

Fig. 7. Variation of mean strain (between alloy variants GA1 and GA3) with % fatigue life (a) Stress-levels: 150, 180 & 270 MPa (b) Magnified view showing the stress-levels 150 & 180 MPa.

more in the former case enabling a higher plastic deformation compared to the latter.

3.4. Fracture surface investigation and microstructural characterization

Fracture surfaces of selected failed specimens are investigated through SEM. The fracture surfaces of the different alloy variants (GA1 and GA3) failed under fatigue testing are shown in Figs. 8-11. Please refer to Table 2 for the specimens that are chosen for fractographic investigation. It is also important to note that fatigue crack initiation is found to take place in big recrystallized grains at the edge (surface). This is found to hold true irrespective of the alloy variants GA1 and GA3 for all the failed specimens. The fatigue test data show strong resemblance between GA2 and GA3. Therefore, for fractographic and metallographic investigations, only alloy variants GA1 and GA3 are considered. However, fractographic analysis pertaining to GA2, carried out at stresses 270 and 180 MPa, is presented in the Appendix A (see Fig. A2) which shows features similar to that observed for GA3.

3.4.1. Influence of applied stress

To understand the influence of applied stress on fracture mechanisms, two stress levels are chosen (a) 270 MPa and (b) 180 MPa for a particular alloy variant (GA3) (Figs. 8-9).

The overall fracture surface of the specimen failed at 270 MPa (Alloy variant: GA3, N_f: 45,114) is shown in Fig. 8(A) marking the crack initiation (I), crack propagation (II) and the overload failure (III) region. Magnified image of marked portion B from Fig. 8(A) shows the crack initiation and propagation region in more detail. The cracks seem to originate from multiple sites (the initiation region is marked in Fig. 8 (B)). However, the direction of crack propagation becomes similar after the early stage of crack propagation (marked as II-1 in Fig. 8(B)) is over. This indicates that the cracks gradually coalesce to form the major Stage-II crack (marked as II-2 in Fig. 8(B)) which propagates to failure. Marked portion C from Fig. 8(B) shows the crack initiation zone to be a faceted, featureless region, indicating transgranular crack initiation. River-markings (which are indications of transition from Stage-I to Stage-II crack [35]) are observed to appear from the initiation zone (marked by yellow arrows in Fig. 8(C)) which gradually widen further with fine striations forming within (marked by white arrows Fig. 8(C)), indicating the transition from Stage-I to Stage-II crack.

The fracture surface of the specimen failed at 180 MPa (Alloy variant: GA3, N_f: 261,332) is shown in Fig. 9 (A), marking the crack initiation and crack propagation regions. Marked portion B shows the crack initiation and propagation regions in more detail. Contrary to what observed for 270 MPa (Fig. 8(B)), a singular crack initiation site is observed in this case (Fig. 9(B)). The crack is found to initiate (marked by red arrow in Fig. 9(B)) within a large recrystallized grain (300 μm, marked by yellow arrow) indicating that the nature of crack-initiation is transgranular. This also indicates that the among all the recrystallized grains at the edge, the bigger ones are the preferred sites for fatigue crack initiation The crack propagates further across the grain-boundary indicative of transgranular crack propagation.

Fig. A2 –which corresponds to variant GA2- shows a similar trend to that found in GA3, with multiple crack-initiation sites at 270 MPa and singular crack-initiation site at 180 MPa.

3.4.2. Influence of alloy variant

To understand the influence of impurity content on fracture mechanisms and subsequent fatigue life, fracture surfaces are compared between the alloy variants GA1 and GA3 across the stress levels (a) 270 MPa and (b) 150 MPa (Figs. 10-11). It is important to choose 150 MPa since fatigue testing at this stress level led to the occurrence of run-out for GA1 in contrast to a finite fatigue life for GA3.

The overall fracture surface of the specimen failed at 270 MPa (Alloy variant: GA1, N_f: 65159) is shown in Fig. 10(A) marking the crack initiation, crack propagation and the overload failure region. Marked portion B shows the initiation and propagation region in more details. Rather than multiple crack initiation observed in Fig. 8(B) for GA3, crack seems to originate from a singular site in this case. The small overall fatigue failure region (crack initiation + crack propagation, marked as I + II in Fig. 10(A)) is indicative of rapid Stage-II crack propagation, which also commensurate with the cyclic softening/high strain accumulation at this stress level (see Fig. 7). To reveal further details, the marked portion C shows the featureless Stage-I crack initiation zone (marked in red) and the transition zone between Stage-I and Stage-II wherein fine striations appear (marked by black arrows). Fatigue striations (measured at a distance of 4 mm from the initiation region) indicative of Stage-II crack propagation is observed in Fig. 10(D), along with presence of secondary cracks and fine dimples (marked in the figure). Fig. 10(E) shows the overload failure region in detail indicating presence of dimples typical of a ductile failure.

The fracture surface of specimen failed at 150 MPa (Alloy variant: GA3, N_f: 1,364,986) is shown in Fig. 11 (A) marking the crack initiation (marked as I), early-stage crack propagation (marked as II-1) and Stage-II crack propagation region (marked as II-2). Marked portion B shows the crack initiation region to be intergranular where the entire grain boundary facet of a recrystallized grain is visible. To reveal further details, marked portion C and D from Fig. 11(B) are magnified. Fig. 11(C) shows clearly cracking along the grain boundary. Additionally, several intermetallic particles are found to anchor the grain boundary. Fig. 11 (D) shows the intergranular crack more clearly, along with an intermetallic particle at the interface (note that the particles are previously

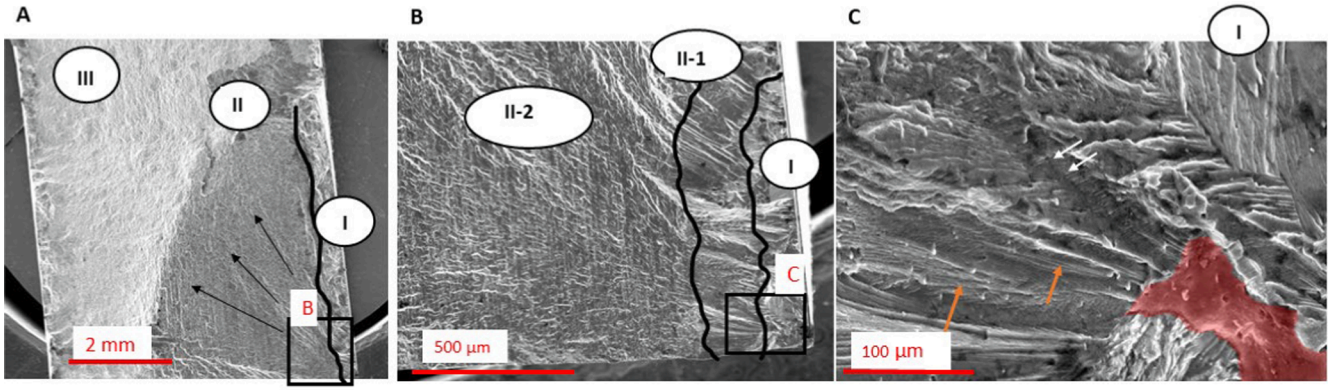

Fig. 8. SEM images pertaining to fracture surface of the specimen tested at 270 MPa (Alloy variant: GA3) showing (A) the overall fracture surface, I: crack initiation region, II: crack propagation, III: overload failure, black arrows mark direction of crack propagation (B): crack initiation and propagation in detail, II-1: early stage crack propagation, II-2: Stage-II crack propagation (C) crack initiation zone (marked in red), with river-markings (marked by orange arrows) and fine striations (marked by white arrows).

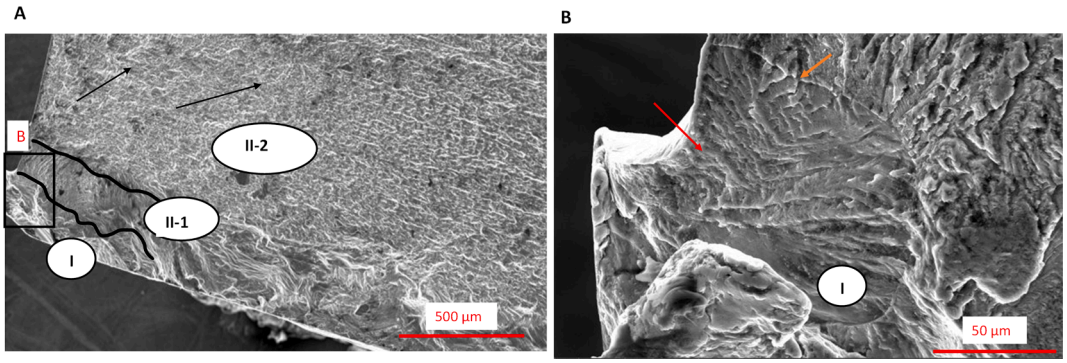

Fig. 9. SEM images pertaining to fracture surface of the specimen tested at 180 MPa (Alloy variant: GA3) showing (A) crack initiation and propagation, I: crack initiation region, II-1: early stage crack propagation, II-2: Stage-II crack propagation (B) crack initiation (marked by red arrow) from a big recrystallized grain (marked by orange arrow).

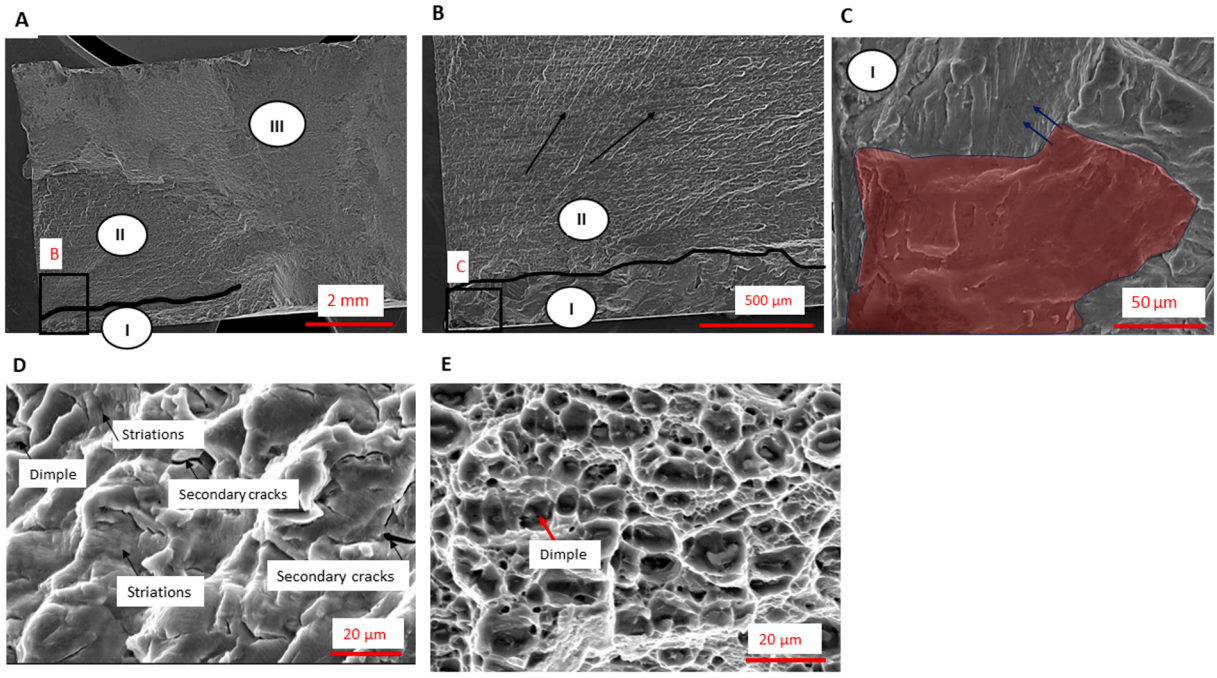

Fig. 10. SEM images pertaining to fracture surface of the specimen tested at 270 MPa (Alloy variant: GA1) showing (A) the overall fracture surface, I: crack initiation region, II: crack propagation, III: overload failure, (B) Crack initiation and propagation in detail (black arrows mark the direction of crack propagation) (C) Stage-I crack initiation (zone marked in red) and transition to Stage-II (fine striations marked by blue arrows) (D) Stage-II fatigue crack propagation zone in detail (E) Overload failure zone in detail showing dimples (ductile failure).

identified through EDS analysis as Al-Fe-Mn-Si intermetallics, see Table 4) which suggests possible decohesion of the particle from the interface of the grain boundary, leading to the initiation of intergranular crack. Size of the particle is-2 µm which corresponds well with particle size and distribution elaborated in Table 3(b) and Fig. 4. It may be recalled that the cyclic strain is lowest at 150 MPa, among all the stress levels in GA3 (Fig. 7), indicating the possibility of a meagre plastic deformation. In such a case, rather than transgranular crack initiation from the surface through formation of persistent slip band (PSB), nucleation of cracks from the breaking of particles located at the grain boundary can be favored. To further corroborate this claim, the side-view of the specimen perpendicular to the crack-plane is observed (fracture surface) is observed and similar intergranular cracking (secondary) along the recrystallized grains are found. This is shown in Fig. 11 (E) where a wedge-type cavitation is found to occur around an elliptical particle anchoring the grain boundary. The cavity, which possibly emerge from the decohesion of the particle from the grain boundary, nucleates into a crack which propagates along the grain boundary. The above findings coincide with the observations made in Fig. 11(F) which shows the early crack propagation zone in more details. The crack which is initiated along the grain boundary (refer Fig. 11(A)) is found to propagate in a mixed mode, with signatures of both trans – and intergranular crack crack propagation (red arrows indicate the direction of crack propagation). This is confirmed further from Fig. 11(G), which shows Stage-II fatigue crack propagation in the extruded region, marked by striations alongside significant secondary intergranular cracks.

4. Discussion

Cyclic deformation is characterized mainly by the occurrence of slip irreversibility which results from dislocation glide along different paths in the forward and backward cycling [37]. This leads to formation of slip markings at the surface which gradually deepens due to localization of plastic (shear) strain, leading to formation of PSB which is the precursor of fatigue crack [36–38]. Mughrabi [36–38] has shown that slip

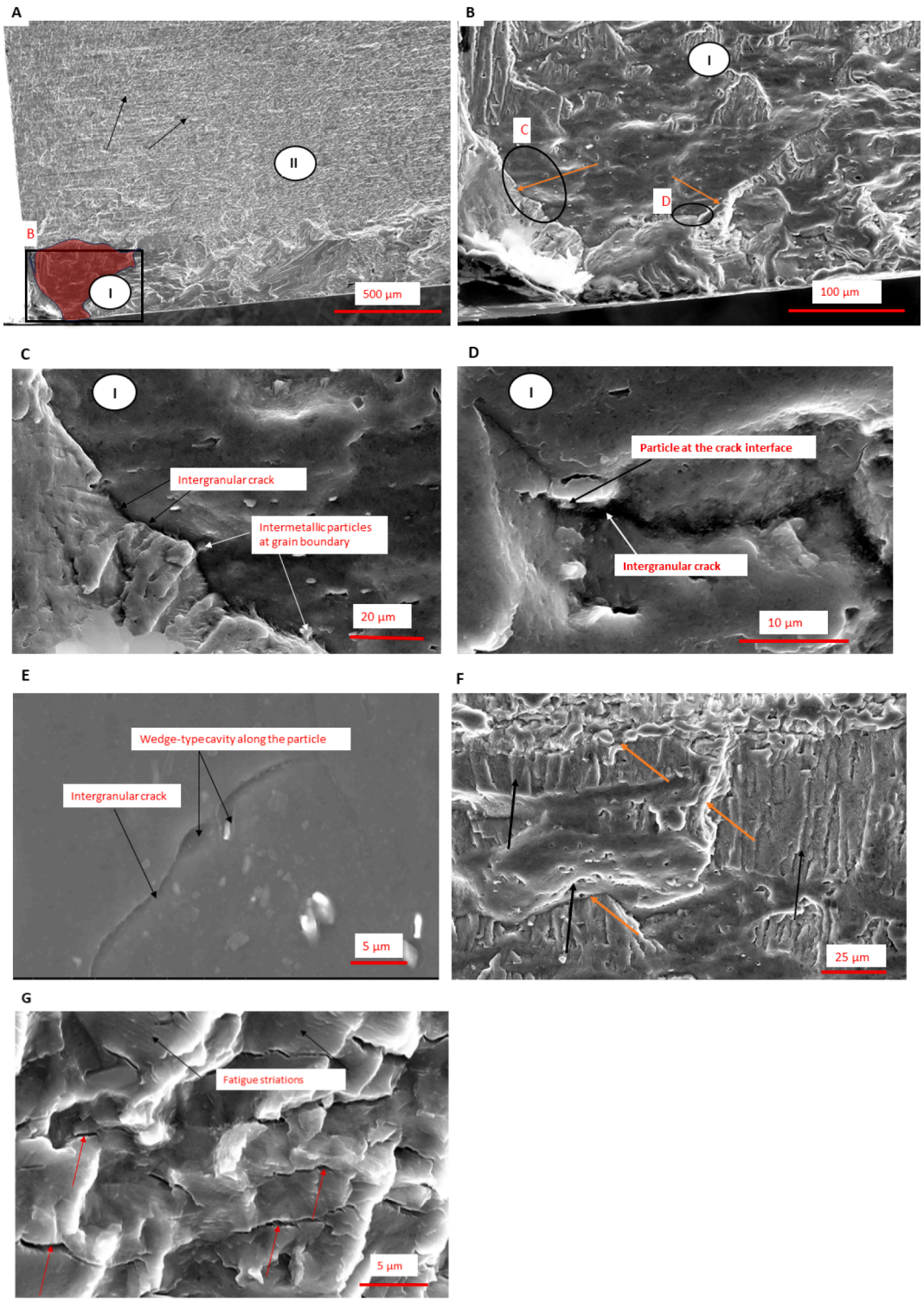

Fig. 11. SEM images pertaining to fracture surface of the specimen tested at 150 MPa (Alloy variant: GA3) showing (A) the overall fracture surface, I: crack initiation region (zone marked in red), II-1: early stage crack propagation, II-2: Stage-II crack propagation (B) intergranular crack initiation (C)-(D) different features of the intergranular crack initiation (E) Side-view perpendicular to the crack plane of the fracture surface, showing wedge-type cavitation along the particle, leading to intergranular crack (F) early stage crack propagation region (black arrows denote direction of crack propagation) in more detail (G) Stage-II crack propagation region showing fatigue striations and intergranular cracks (marked by red arrows).

irreversibility can be measured in terms of plastic shear strain and there is a threshold value of cumulative plastic shear strain for the formation of PSB. The cumulative plastic strain threshold essential to form a PSB at surface through irreversible slip in every cycle, is a function of various parameters like stacking fault energy, applied stress, initial microstructure (dislocation density, presence of precipitate/intermetallic etc) [36–38].

4.1. Influence of applied stress

Al-alloys have an fcc structure and normally a high stacking fault energy which makes it easier to cross-slip under cyclic deformation [39]. However, the ability to cross-slip depends on the nature of cyclic deformation and the stress associated with it. For example, cross-slip will be favored more during LCF wherein a gross plastic deformation occurs [40]. The stresses associated in such scenarios are essentially higher than YS wherein more slip systems are activated, and a greater number of grains are favorably oriented for plastic deformation via slip [40]. However, putting this into perspective of the present case, it seems occurrence of irreversible slip is quite easier at stresses like 270 MPa, even though it is lower than YS (13 % lower for GA1, 17 % lower for GA3). This is corroborated from the high amount of cyclic softening observed (for both GA1 and GA3, see Fig. 7), and multiple crack-initiation sites for GA3 (see Fig. 8) at 270 MPa. On the other hand, when the stress levels are lowered (180–150 MPa, 42–52 % lower than YS for GA1, 45–54 % lower than YS or GA3), the traits are more similar to typical HCF associated with poor slip irreversibility leading to localized plastic deformation. This also follows from the small cyclic hardening with long period of cyclic saturation (both for GA3 and GA1, see Fig. 7)/single crack-initiation site (for GA3, see Fig. 9) observed at 180 MPa. The above discussion therefore makes it clear that nature of cyclic deformation at stresses like 270 MPa is characterized by an inherent global character unlikely of stresses within the HCF regime, contrary to a local character at stresses like 180–150 MPa (irrespective of the alloy variant). This transition from global to local character as a function of stress leads to a strong sensitivity of stress to nature of cyclic deformation, which is typically not expected when the stresses are within the HCF regime. This could be attributed to a sharp change in slip character from multiple-slip tendency to single slip between 270 MPa to 180–150 MPa. This leads to higher slip irreversibility at 270 MPa, compared to 180–150 MPa. Consequently, the threshold value of the plastic strain needed for PSB formation could be reached earlier for 270 MPa, compared to 180–150 MPa.

4.2. Influence of alloy variant

To understand the difference in nature of cyclic deformation and fatigue properties between the different variants, the role of the initial microstructure must be considered. The trend in statistical fatigue life is found to be lower in GA3 compared to GA1, irrespective of applied stress, despite the fact that the tensile properties (YS & UTS) are found to be higher in GA3 compared to GA1. It may be noted that content of impurity elements like Fe, Zn and Cu are increased in GA3 compared to GA1. This suggests that the ease of slip associated with fatigue cycling (which depends on stacking fault energy and thereby chemical composition [19]) might be widely different for the above two variants. To corroborate this claim, EBSD inverse pole figure (IPF) maps (superimposed with grain boundary, >2°) and the corresponding distribution of Schmid factor (histogram), pertaining to GA1 and GA3 are presented in Figs. 12-13. The EBSD analysis was performed only at the edge considering the fact that fatigue crack initiation takes place only from the recrystallized grains, which populate the edge region. The IPF maps (Fig. 12 (a) & (b)) show the recrystallized grains in detail, with each grain marked in a uniform color shade indicating specific crystallographic orientation for the same. The corresponding distribution of Schmid factor show the propensity to slip for each grain, with a higher Schmid factor indicating a higher tendency towards slip. The histograms showing the distribution of Schmid factor (Fig. 13) among different grains indicate that recrystallized grains in GA3 have a higher Schmid factor compared to GA1. This is also corroborated by comparing the number density of grains among GA1 and GA3 having higher Schmid factor; the distribution shows that the maximum number of grains having a high Schmid factor like 0.43 is ~0.35 in GA3, as opposed to ~0.2 for a Schmid factor of 0.39 in GA1. These observations indicate that the ease of slip or tendency of cross-slip will be favored more in GA3 compared to GA1 under fatigue cycling, notwithstanding the effect of different applied stresses, resulting in higher slip-irreversibility and an early PSB formation (crack-initiation) in the former case. This leads to lower statistical fatigue life in GA3 compared to GA1 (Fig. 6). At higher values of stresses (like 270 MPa), cross-slip may be favored irrespective of alloy variants (also mentioned in section 4.1), which is unlikely at lower stresses. This could explain why the difference the fatigue life between GA1 and GA3 gradually widens with the lowering of stress-level (see Fig. 6).

It may be noted that the EBSD images that are shown in Figs. 12-13 are representative of the cases considered viz. alloy variants GA1 and GA3. To ensure reliability of the data, additional EBSD scans are performed on both the alloy variants GA1 and GA3 which show recrystallized grains with different crystallographic orientations (similar to that

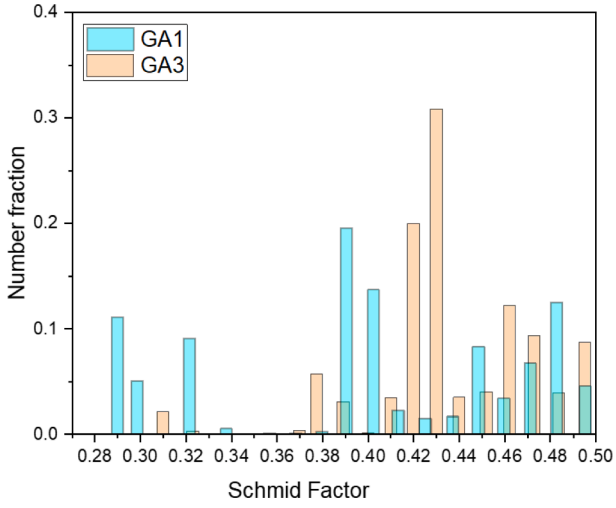

Fig. 13. Histrogram showing Schmid factor distribution in different grains in GA1 and GA3.

Fig. 12. EBSD inverse pole figure (IPF) maps (superimposed with grain boundary, >2°) at the edge (surface) (a) GA1 (b) GA3.

observed in the earlier scans). These results are included in the Appendix A in Fig. A3.

Although the difference in trend in fatigue properties between GA1 and GA3 can be explained based on the above discussion, the fracture surface observations suggest that fatigue crack initiation mechanism changes entirely in the alloy variant GA3 compared to GA1 at a lower level of stress like 150 MPa wherein intergranular crack initiation is facilitated in the former case as opposed to a transgranular crack initiation in the latter one. The intergranular crack initiation possibly resulted from the decohesion of the intermetallic particles at the interface of the grain boundary due to a high strain incompatibility at the particle–matrix interface. The particles anchoring the boundary of the recrystallized grains are normally hard compared to the matrix, which leads to high strain incompatibility at those interfaces, under cyclic stressing. To understand why such strain incompatibility arising at the interface of the particle and matrix along the grain boundary drives the crack initiation (in an integranular fashion), it is important to consider the level of the applied stress (150 MPa). It is already discussed that such low levels of stresses are characterized by single slip tendency wherein slip irreversibility is poor. Moreover, new dislocations are generated more favorably during the course of cycling in the recrystallized grains in the surface layer since they are strain-free with very low dislocation density [41]. These dislocations glide towards the grain-boundary and gets arrested there. The poor slip irreversibility at 150 MPa makes it difficult for these dislocations to move across the grain boundary through cross-slip. This is evident from the initial cyclic hardening tendency at 150 MPa (GA3) followed by a long saturation (see Fig. 7). The existing strain-incompatibility at the particle-grain boundary interface is therefore augmented further due to the dislocation pile-up at those grain-boundaries. Such high strain compatibilities cannot be relaxed easily by plastic deformation on neighboring grains due to poor slip irreversibility at 150 MPa. This leads to nucleation of crack at the interface of the particle and grain-boundary, which grows further along the grain boundary under successive cycling (see Fig. 11 (iii)-(iv)). Subsequent crack propagation takes place in a mixed-mode fashion initially, followed by final crack propagation in a transgranular manner (see Fig. 11(v)). The fact that this type of intergranular crack initiation mechanism is observed only for GA3 and not in GA1 (at 150 MPa) can be explained on the basis of the number density of intermetallic particles in the recrystallized surface layer which is almost twice for GA3 when compared to GA1 (see Table 3). This enhances the probability of such intergranular crack initiation in GA3 to a great extent compared to GA1. As a result, finite failure is observed in case of GA3 (1364986) compared to run-out for GA1, at 150 MPa. This is also the reason why a lower fatigue limit (120 MPa) is obtained for GA3 compared to GA1 (150 MPa).

It is also important to note that intergranular crack initiation is observed only at 150 MPa and not at higher stresses like 180–270 MPa wherein transgranular crack initiation is observed (in GA3). The amount of cyclic softening at 270 MPa is remarkably high wherein the cyclic plastic deformation has a global character, thus favoring transgranular crack initiation through PSB formation over integranular crack initiation at the grain-boundary. At 180 MPa, albeit cyclic plastic deformation having a local character, the (cumulative) slip irreversibility throughout the course of cycling may be enough to reach the threshold plastic strain required for PSB formation (transgranular crack initiation) before crack nucleates at the interface of the particle and grain-boundary. As discussed earlier, this follows from the strong stress-dependence of slip irreversibility which will be slightly higher at180 MPa compared to 150 MPa. Therefore, the possibility that the dislocations can escape the grain-boundary barriers (potentially anchored by particles) through cross-slip, will be more at 180 MPa compared to 150 MPa. This offsets the strain-incompatibility at the particle-grain boundary interface to some extent at 180 MPa, compared to 150 MPa.

The above phenomenon is depicted schematically in Fig. 14 by comparing two stress levels (270 & 150 MPa) among the alloy variants GA1 and GA3. At a high stress of 270 MPa in GA3, cross-slip allows high dislocation mobility among the grains. This leads to absence of dislocation pile-up at grain boundary and favors PSB formation at the surface, and thereby transgranular crack initiation (marked by the blue arrow). On the other hand, at 150 MPa in GA1, even though dislocation pile-up could form at the grain boundary, low number density of intermetallic particles reduces chances of strain-incompatibility at the particle–matrix interface that could facilitate an intergranular crack initiation. All the above factors are satisfied at 150 MPa in GA3, wherein dislocation pile-up coupled with strain-incompatibility at the particle–matrix interface (due to a high number density of primary particles) favored intergranular crack initiation (marked by blue-arrows).

4.3. Comparison between tensile and fatigue properties

It is also interesting to note that the trend in tensile and fatigue properties vis-à-vis the alloy variants are exactly the opposite. The intermetallic particles which are found to act as potential crack initiation sites at 150 MPa for the alloy variant GA3 (based on the discussion above) are also the primary strengtheners in this Al-alloy [42,43]. During the course of plastic deformation under tensile loading, these particles resist the dislocation motion by acting as obstacle to dislocation glide, leading to “precipitation strengthening” [19]. The extent of “precipitation strengthening” by the particles will depend on their number density. A higher number density of particles in the alloy variant GA3 (both in edge and centre) compared to that in GA1 (see Table 3(b)) indicates a higher extent of “precipitation strengthening” in the former case, resulting in a higher YS and UTS therein compared to the latter. Precipitation strengthening occur in a similar manner under HCF- however, particle number density only at the edge should be considered in this case since fatigue crack is always found to initiate from big recrystallized grains at the edge (surface). The average particle number density at the edge remains higher in GA3 compared to GA1, which indicates the possibility that “precipitation strengthening” by the particles will be higher in GA3 rather than GA1 during HCF. However, given the fact that the plastic deformation under HCF is highly localized, several other factors like favorable orientation of the grains for slip, ease of cross-slip for individual grains needs to be considered apart from “precipitation strengthening” by the particles. In such a scenario, it is possible that the grain(s) at the edge which are conducive for slip may have lower particle number density and therefore the extent of “precipitation strengthening” by the particles in mitigating fatigue damage might be insignificant. This probability is even more when the stress is lower, since the plastic deformation is found to change from global to local character in this alloy (irrespective of alloy variant) with lowering in stress. This makes propensity to slip/ease of cross-slip the major factor that governs the fatigue properties, rather than “precipitation strengthening” by the particles. Consequently, the fatigue properties are poorer in GA3 with lower statistical fatigue life compared to GA1 (please see the discussion made with respect to Schmid factor maps in section 4.3 for explaining the difference in fatigue properties between the variants GA1 and GA3). The above arguments do not apply for tensile loading wherein bulk deformation takes place and local nature of deformation in individual grains remains inconsequential- which makes “precipitation strengthening” by the particles the major factor that governs the monotonic properties. It should be noted that any concrete conclusions for addressing the role of impurities on tensile properties requires further experimental analysis as in this work, only one specimen is tested under static load and the major focus is on fatigue performance of the studied alloys.

4.4. Fracture and damage mechanism map

The above discussion envisages a competitive damage mechanism under cyclic deformation as a function of stress, with possibility of intergranular crack initiation on one hand (governed by strain

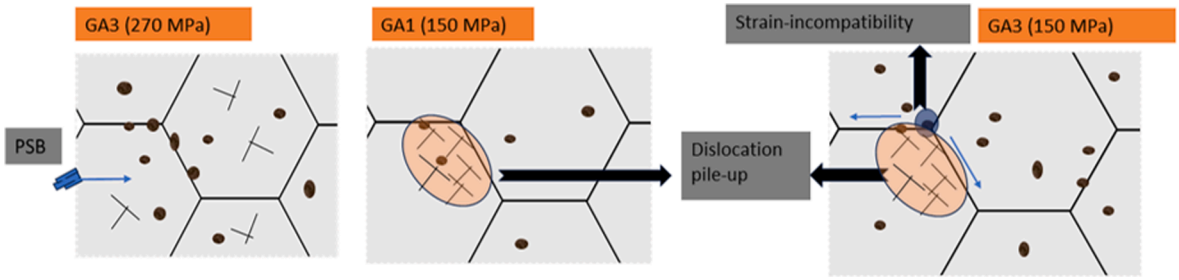

Fig. 14. Schematic showing the mechanism of different type of crack initiation (trans and intergranular) among alloy variants GA1 and GA3 relative to stress level.

incompatibility at the particle-grain boundary interface)-and transgranular crack initiation on the other (governed by irreversible plastic slip). These aspects are extended further through a fracture and damage mechanism map incorporating all the alloy variants (GA1-GA3) and stress levels (120–270 MPa) superimposed on the stress-life curve, shown in Fig. 15. Please note that the map is based on fracture surface observations for all alloy variants and stress levels, which are not presented in the paper. The map brings out the changes in fracture mechanisms as a function of stress and alloy variant. For alloy variants GA2 and GA3, intergranular crack initiation governed by strain incompatibility at the particle-grain boundary interface is favored at lower levels of stresses (150 MPa) whereas transgranular crack initiation is favored at higher stresses (180–270 MPa). However, the nature of (transgranular) crack initiation irrespective of the alloy variant, is strongly affected by the change in slip character manifested as a difference in nature of cyclic plastic deformation. Multiple slip/cross-slip tendency marked by a global character of cyclic plastic deformation is prominent at 270–220 MPa. Single-slip tendency marked by a local character of cyclic plastic deformation is prominent at a stress of 180 MPa.

4.5. Role of different microstructural attributes on fatigue properties

Fatigue properties in a polycrystalline material depends on several microstructural attributes viz. grain-size, grain orientation, stacking fault energy, presence of second phases/particles/precipitates [36–38]. Fatigue life is governed by the relative role of one or more of these attributes depending on the initial microstructure and the applied stress.

The initial microstructure in this alloy is hierarchical in nature irrespective of the alloy variant. A layer of recrystallized grains is found in the edge with a wide variation in grain size from as big as ~340 μm to as low as ~20 μm, followed by smaller extruded grains which vary in size from ~3 μm to ~65 μm (see Fig. 3). Bigger grain-size facilitates early localization of slip and is therefore detrimental for the life spent in fatigue crack initiation. This is reflected in the present work wherein fatigue cracks are found to initiate from bigger recrystallized grains in the surface (edge), irrespective of stress and alloy variants. The influence of grain orientation can be highlighted through texture analysis- however, this is not considered in the present work. Nevertheless, it is important to note that a variation in texture among the alloy variants can lead to difference in fatigue properties especially when the stresses are lower and fewer grains conducive for slip are available. In a similar manner, variation in stacking fault energy- which is a function of chemical composition of the material- can also lead to change in fatigue properties. Increase in stacking fault energy facilitates chances of cross-slip and thereby deteriorates fatigue properties [19]. Putting this in perspective of the present work, variation in chemical composition between the alloy variants GA1 and GA3 in terms of impurity content like Fe, Cu and Zn could lead to variation (increase/decrease) in stacking fault energy among the above variants. This, in turn, could lead to change in slip character (tendency of cross-slip) – reflected from the Schmid factor map which shows higher tendency of cross-slip in GA3 compared to GA1 (Fig. 13)- eventually resulting in different fatigue properties among the above variants, relative to stress. The presence of primary particles- which contributes to "precipitation strengthening" in 6xxx series of Al-alloys [42,43]- is found to be a major detriment for the fatigue properties, especially at very low stresses like 150 MPa. The present work showed that a higher number density of these intermetallic particles in GA3 compared to GA1 favored intergranular crack initiation leading to poorer fatigue properties in the former case.

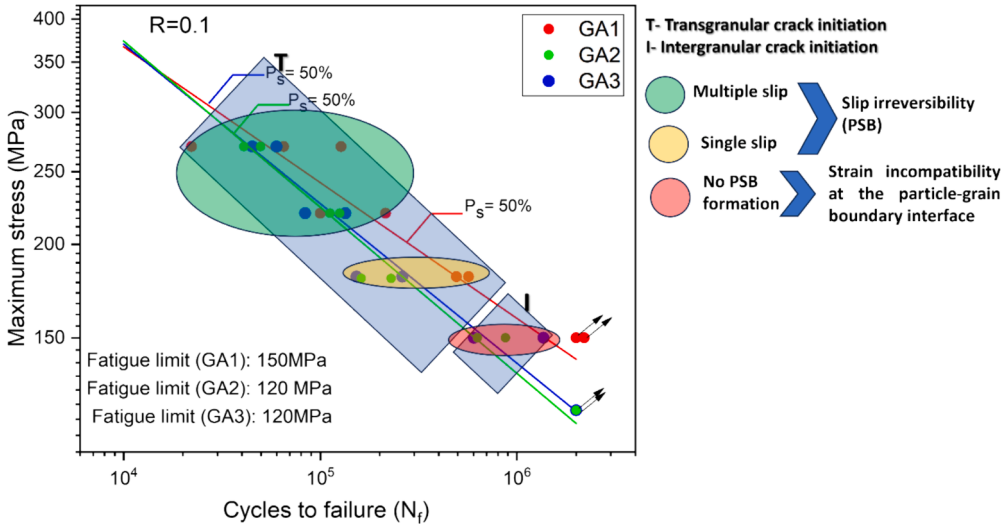

Fig. 15. Fracture and damage mechanism map superimposed on the stress-life curve depicting the different failure mechanisms under HCF as a function of stress-level and alloy variant. T: Transgranular, I: Intergranular.

The arguments made above clearly highlights the role of different microstructural attributes like grain-size, stacking-fault energy, and number density of intermetallic particles in deciding the fatigue properties. Considering the change in nature of deformation from global to local with lowering in stress, it is not possible to identify one single attribute as the primary contributor to fatigue damage. Instead, the relative role of the above microstructural attributes can decide the extent of fatigue damage- which again can vary with change in stress- which is also depicted from the map presented in Fig. 15.

It is also expected that the microstructural attributes like grain-size, composition of particles/phases along with their size, morphology, and distribution will vary depending on the processing condition viz. as-cast condition with/without homogenization treatment vis-à-vis extruded condition, T6 aging vis-à-vis T4 aging etc. Even though performing the experimentation in respect to the points made above is beyond the scope of the present work, this is a potential ground of future research which will serve as premise for developing microstructure or physics based numerical fatigue life-prediction methodologies in future.

5. Summary and outlook

The study, based on conducting high cycle fatigue tests on three different alloy variants of Al-alloy with increased order of impurity content, showed that fatigue properties were poorer in variants with high impurity content viz. GA2/GA3 (lower fatigue limit) compared to that with less impurity content viz. GA1 (higher fatigue limit). This was attributed to a lesser slip-damage (lower tendency of cross-slip) under fatigue cycling in the former case-due to a possible change in stacking fault energy- compared to the latter. Fatigue behavior is found to be strongly stress-sensitive marked by a change in the nature of cyclic plastic deformation from global to local character (with change in slip character from multiple to single slip tendency) with subsequent lowering of stress levels. Fatigue fracture is found to be primarily transgranular (with crack initiating from the big recrystallized grains at the surface) except at very low stress like 150 MPa wherein intergranular crack initiation is observed marked by possible decohesion of intermetallic particle at the interface of the grain boundary, owing to the high strain incompatibility at the particle–matrix interface. Such occurrence is found only in GA3 in contrast to run-out in GA1, due to a higher number density of intermetallic particles in the recrystallized surface layer in GA3 compared to GA1- which enhanced the probability of intergranular crack initiation in the former case. The above aspects are expressed through a fracture mechanism map which bings out the competitive damage mechanism under cyclic deformation as a function of stress and alloy variant.

The lower fatigue limit found in GA2/GA3 compared to GA1 in this study, brings out the detrimental effect of impurities on fatigue properties and therefore indicated that the alloy variant GA1 is more suitable for fatigue-sensitive applications. The strong stress-sensitivity of the underlying mechanisms responsible for fatigue deformation, is found to be independent of the alloy variants and therefore, must be an inherent character in this alloy. This aspect must be accounted for in designing against HCF, since high amount of cyclic softening under HCF cycling is not a desirable trait and can have detrimental effect on the structural integrity of the components. Considering the deleterious role played by the primary intermetallic particles at lower levels of stresses like 150 MPa and only in GA3, stress-sensitivity must be accounted for while tailoring the microstructure through different types of precipitates/intermetallic particles for improving the fatigue strength.

CRediT authorship contribution statement

Aritra Sarkar: Writing – original draft, Methodology, Investigation, Formal analysis, Data curation, Conceptualization. **Mehmet Aktunali:** Investigation. **Siri Marthe Arbo:** Resources, Investigation. **Jon Holmestad:** Investigation. **Luigi Mario Viespoli:** Writing – review & editing. **Bård Nyhus:** Writing – review & editing, Resources. **Geir Ringen:** Writing – review & editing, Resources. **Nima Razavi:** Writing – review & editing, Resources, Methodology, Conceptualization.

Declaration of competing interest

The authors declare that they have no known competing financial interests or personal relationships that could have appeared to influence the work reported in this paper.

Data availability

Data will be made available on request.

Acknowledgement

This work has been funded by the Aluminium Green Platform, AluGreen (contract number 328843). The authors gratefully acknowledge the financial support from the Research Council of Norway and the partners of the AluGreen, especially Norsk Hydro Aluminium, Sunndal for supplying the material for the performed tests. Ms. Linda Irene Tverfjell from Hydro is gratefully acknowledged for acquiring the optical microstructure image of the as-extruded profile.

Appendix A

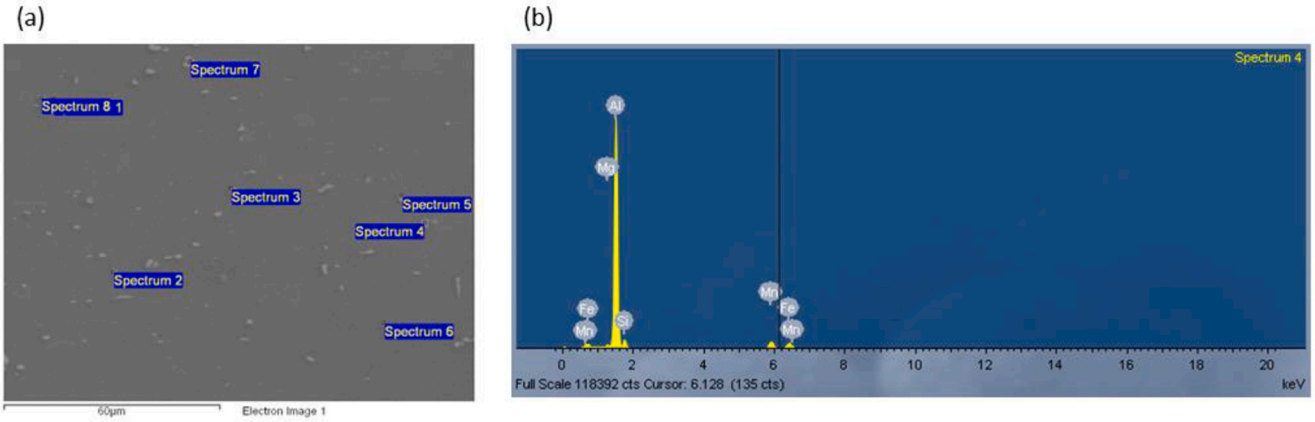

Fig. A1. (a) SEM image pertaining to the alloy variant GA1 showing the eight locations of EDS spectra (b) Image corresponding to spectrum 4

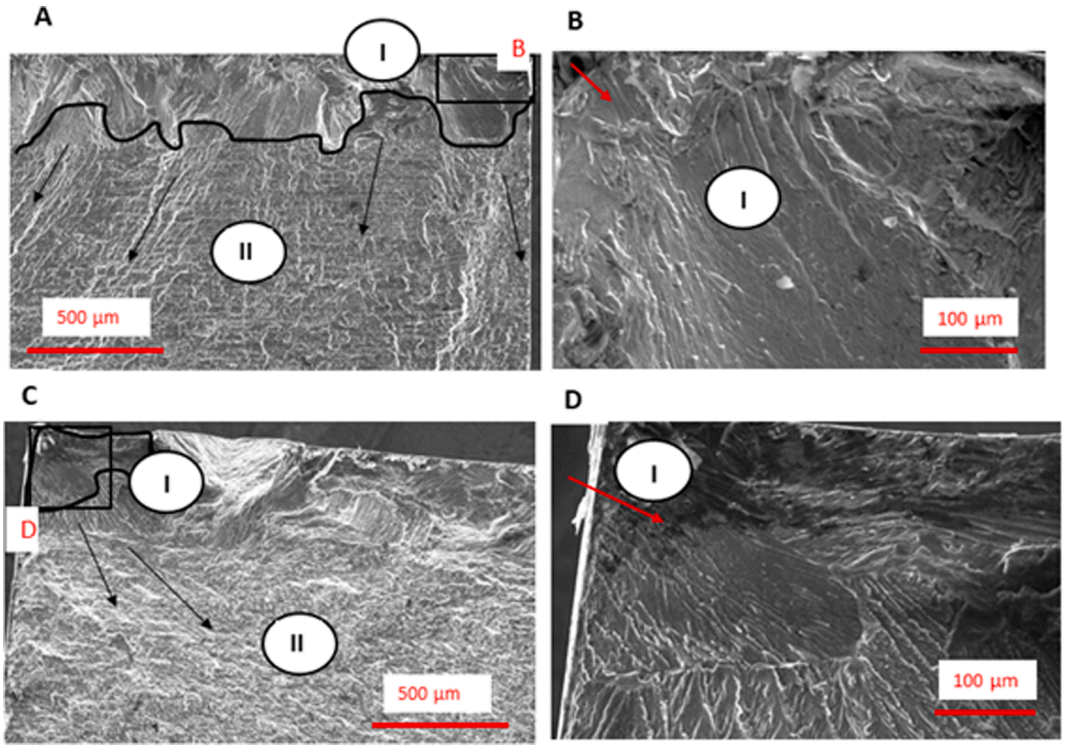

Fig. A2. SEM images of the fracture surface of the specimen tested at (A)270 MPa (C) 180 MPa (Alloy variant: GA2) showing (A), (C): crack initiation and propagation region (black arrows mark direction of crack propagation), (B), (D): magnified images showing details of the crack initiation region (marked by red arrow). I: crack initiation region, II: crack propagation

Fig. A3. EBSD inverse pole figure (IPF) maps (superimposed with grain boundary, >2°) at the edge (surface) (a) GA1 (b) GA3

Appendix B. Supplementary material

Supplementary data to this article can be found online at https://doi.org/10.1016/j.ijfatigue.2024.108406.

References

[1] Bushi L. EDAG Silverado Body Lightweighting Final LCA Report, Aluminum Association; 2015.
[2] European Aluminium, 2015 Sustainability Highlights, Reporting on the European aluminium industrys performance, European Aluminium; 2017.
[3] Polmear IJ. J. Light alloys. Oxford: Butterworth-Heinemann; 2006.
[4] Dixit M, Mishra RS, Sankaran KK. Structure–property correlations in Al 7050 and Al 7055 high-strength aluminum alloys. J MaterSci Eng A 2008;478:163–72.
[5] Ferrarini CF, Bolfarini C, Kiminami CS, Botta WJF. Microstructure and mechanical properties of spray deposited hypoeutectic Al–Si alloy. J MaterSci Eng A 2004;377:577–80.
[6] Gutowski T, Sahil S, Allwood J, Ashby M, Worrell E. The energy required to produce materials: constraint on energy intensity improvements parameters of demand. Phil Trans Royal Soc A 2013;371:20120003.
[7] Das SK, Kaufman JG. Recycling aluminum aerospace alloys. Light Metals. Annual Meeting & Exhibition. TMS, Orlando; 2007. p. 1161–1165.
[8] Stacey M. Aluminium recyclability and recycling towards sustainable cities. Cwningen Press, International Aluminum Institute, Nottingham; 2015.
[9] Xiao Y, Reuter MA. Recycling of distributed aluminum turning scrap. Miner Eng 2002;15:963–70.
[10] Soo V, Peeters J, Compston P, Doolan M, Duflou J. Economic and environmental evaluation of aluminium recycling based on a Belgian case study. Proc Manuf 2019;33:639–46.
[11] Ingarao G, Baffari D, Barcquene E, Fratini L, Duflou D. Energy demand reduction of aluminum alloys recycling through friction stir extrusion processes implementation. Proc Manuf 2019;33:632–8.
[12] Taylor JA. The effect of iron in Al-Si casting alloys. Proc 35th Australian Foundry Inst Natl Conf 2004:148–57.
[13] Eva Tillová, Mária Chalupová, Lenka Hurtalová, "Evolution of Phases in a Recycled Al-Si Cast Alloy During Solution Treatment", Scanning Electron Microscopy (Ed: Viacheslav Kazmiruk), Intech Open Publishers, 2012, UK.
[14] Dinnis CM, Taylor JA, Dahle AK. Porosity formation and eutectic growth in Al-Si-Cu-Mg alloys containing iron and manganese. Proc 9th Intl Conf Al-alloys 2004:1016–21.
[15] Caceres CH, Svenson IL, Taylor JA. Strnegth-ductility behavior of Al-Si-Cu-Mg castings alloy in T6 temper. Int J Cast Metals Res 2003;15:531–43.
[16] Liu Z, Zhou L, Li G. Effects of cooling rate on the microstructure and tensile strength of A356 alloy wheels. In: 3rd International Conference on Material, Mechanical and Manufacturing Engineering (IC3ME 2015), Atlantis Press, Guangzhou, China, 2015.
[17] Beyer T, Ebereonwu D, Koch A, Decker P, Kauws A, Rosefort M, Walther F. Influence of increased Cu and Fe concentrations on the mechanical properties of the EN AB-42100 (AlSi7Mg0.3) aluminum alloy. In: Broek S. (eds) Light Metals 2023, The Minerals, Metals & Materials Series. Springer, TMS 2023, San Diego, California, USA, 2023.
[18] Nicholas T. High Cycle Fatigue: A Mechanics of Materials Perspective, Elsevier Publications, United Kingdom; 2006.
[19] George E. Dieter, Mechanical Metallurgy, McGraw Hill Book Company, United Kingdom; 1988.
[20] Kim HJ, Kobayashi T, Ito T. Effects of Fe and Ca on usual and impact fatigue characteristics of AC2B-T6 aluminium casting alloy. Mater Sci Forum 1996;217–22:1395–400.
[21] Závodská D, Kucharíková L, Tillová E, Guagliano M, Chalupová M, Uhríčik M, et al. The fatigue lifetime of AlZn10Si8Mg cast alloy with different percentage of iron. Proc Struct Integrity 2018;13:1554–9.
[22] Oh S-H, Kim H-J. Effect of (Ti-B) and Sr additives on impact and fatigue properties of recycled AC4A aluminum casting alloy. J Korea Foundry Soc 2019;39(4):61–74.
[23] Salvo J, Afonso M. Fatigue strength and microstructure evaluation of Al 7050 alloy wires recycled by spray forming, extrusion and rotary swaging. Trans Nonferrous Metall Soc China 2020;30:3195–209.
[24] Koch A, Bonhage M, Teschke M, Luecker L, Behrens B, Walther F. Electrical resistance-based fatigue assessment and capability prediction of extrudates from recycled field-assisted sintered EN AW-6082 aluminium chips. Mater Characterization 2020;169:110644.
[25] Koch A, Wittke P, Walther F. Computed Tomography-based characterization of the fatigue behavior and damage development of extruded profiles made from recycled AW6060 aluminum chips. Mater 2019;12(2372):2–17.
[26] Krolo J, Gudic S, Vrsalovic L, Lela B,Dadic Z. Fatigue and corrosion behavior of solid-state recycled aluminum alloy EN AW 6082. J Mater Eng Perform 2020;29(7):4310–21.
[27] Mathers G. The welding of aluminium and its alloys. CRC Press LLC: Woodhead Publishing Ltd; 2002.
[28] Herring D. Temper designations for aluminum alloys: what they are and why we need to know industrial heating 2012;80(2):20–24.
[29] ASTM International. ASTM E8 / E8M-16a - Standard test methods for tension testing of metallic materials. ASTM International, West Conshohocken, (PA), USA; 2016.
[30] ISO-12107, Metallic materials — Fatigue testing — Statistical planning and analysis of data; 2012.
[31] Lukáš P, Kunz L. Specific features of high-cycle and ultra-high-cycle fatigue. Fatigue Fract Eng Mater Struct 2002;25(8–9):747–53.
[32] Mughrabi H. On 'multi-stage' fatigue life diagrams and the relevant life controlling mechanisms in ultrahigh-cycle fatigue. Fatigue Fract Eng Mater Struct 2002;25(8–9):755–64.
[33] Mughrabi H. Specific features and mechanisms of fatigue in the ultrahigh-cycle regime. Int J Fatigue 2006;28(11):1501–8.
[34] Müller-Bollenhagen C, Zimmermann M, Christ H-J. Adjusting the very high cycle fatigue properties of a metastable austenitic stainless steel by means of the martensite content. Proc Eng 2010;2(1):1663–72.
[35] Wang X, Ma J, Welo T. Influence of deformation prior to ageing on fatigue behavior of extruded AA6082-T6 profiles. Int J Fatigue 2022;162:106990.
[36] Mughrabi H. Microstructural mechanisms of cyclic deformation, fatigue crack initiation and early crack growth. Phil Trans R Soc A 2016;373:20140132.
[37] Mughrabi H, Wang R, Differt K, Essmann U. Fatigue crack initiation by cyclic slip irreversibilities in high-cycle fatigue. In: Fatigue mechanisms: advances in quantitative measurement of physical damage, ASTM STP 811 (eds. J. Lankford, D. L. Davidson, W.L. Morris, R. P. Wei), pp. 5–45. Philadelphia, PA: American Society for Testing and Materials, 1983.
[38] Mughrabi H. Microstructural fatigue mechanisms: Cyclic slip irreversibility, crack initiation, non-linear elastic damage analysis. Int J Fatigue 2013;57:2–8.
[39] Kumar N, Goel S, Jayaganthan R, Brokmeier H-G. Effect of grain boundary misorientaton, deformation temperature and AlFeMnSi-phase on fatigue life of 6082 Al alloy. Mat Charact 2017;124:229–40.
[40] Lukas P, Klesnil M. Cyclic stress-strain Response and fatigue life of metals in low amplitude region. Mater Sci Eng A 1973;11:345–56.
[41] Xiao G, Jiang J, Liu Y, Wang Y, Guo B. Recrystallization and microstructure evolution of hot extruded 7075 aluminum alloy during semi-solid isothermal treatment. Mater Charact 2019;156:1098.
[42] Sha G, Cerezo A. Early-stage precipitation in Al–Zn–Mg–Cu alloy (7050). Acta Mater 2004;52(15):4503–16.
[43] Srivatsan TS. An investigation of the cyclic fatigue and fracture behavior of aluminum alloy 7055. Mater Des 2002;23:141–51.